*Korean J. Chem. Eng.*, 37(1), 166-175 (2020)
DOI: 10.1007/s11814-019-0414-8

pISSN: 0256-1115
eISSN: 1975-7220

# Facile and scalable synthesis of nitrogen-doped ordered mesoporous carbon for high performance supercapacitors

**Lei Fan†, Peizheng Sun, Li Yang, Zhilong Xu, and Jie Han†**

School of Chemistry and Chemical Engineering, Yangzhou University, Yangzhou 225002, China

(*Received 24 August 2019 • accepted 21 October 2019*)

**Abstract**−Nitrogen-doped carbon has been receiving tremendous research interest due to its exotic electrochemical performance and catalyzing capability. Nevertheless, large-scale synthesis of ordered, mesoporous, nitrogen-doped carbon for supercapacitors is rarely reported due to the complexity and uncontrollable property of polymerization of carbon/nitrogen precursors. In this work, we report a facile and efficient approach for mass production of nitrogen-doped carbon, with a narrow pore size distribution and a sheet morphology, via a simple solution casting of biomass-based mixture. Upon drying, the gelatin molecules self-assemble into sheets, and guide the homogeneous loading of sacrificial silica nanospheres. Further carbonization and template removal procedures allow the low-cost production of nitrogen-doped carbon sheets in the absence of complex polymerization. As a result, nitrogen-doped carbon sheets possess a high nitrogen content and ordered, interconnected mesoporous channels, with porosity parameters being carbonization temperature and template size dependence. Additionally, nitrogen-doped, ordered carbon sheets exhibit high performance for supercapacitor application, including high specific capacitances and energy/power densities. This work demonstrates a unique route to synthesizing ordered mesoporous nitrogen-doped carbon sheets via a scalable, low-cost method, which may shed light on many other applications aside from energy storage, such as water splitting, catalysis and sensor.

Keywords: Nitrogen-doped Carbon Sheets, Mesoporous Channels, Supercapacitor, Scalable Route, Energy Storage

## INTRODUCTION

Carbon nanomaterials possess a range of advantages, such as large specific surface area, physiochemical and thermodynamic stability and developed porous channels, being ideal for high-performance energy storage devices, in particular supercapacitors [1-5]. Previous reports have revealed that both the surface chemistry of carbon nanomaterials and porous parameters greatly affect the supercapacitor performance [6-9]. While the pristine carbon showcases a nature of hydrophobicity and thus limits the aqueous electrolyte wettability, the porous channels determine the ion diffusion kinetics [10-12]. Therefore, the capacitance and rate performance of aqueous supercapacitors are surface chemistry and porosity dependent. By adjusting the carbon surface functionalities and/or engineering the pores, the wettability [13,14], electronic conductivity and ionic conductivity [15,16] of the electrode can be improved, leading to enhanced supercapacitor performance.

Unlike the oxidation of carbon, which introduces plenty of hydroxyl groups at the cost of electronic conductivity of the material, nitrogen doping is a promising route to tune the carbon surface chemistries without losing the conductivity [17-20]. This is best evidenced by the fact that nitrogen has a stronger electronegativity than that of -OH groups. As a result, fast surface redox reactions are facilitated on the nitrogen-doped carbon, adding pseudocapacitance to electrochemical double-layer capacitance (EDLC) without deteriorating the rate capability [21-23]. Long et al. synthesized nitrogen-doped mesoporous carbon using melamine and resin as the nitrogen and carbon sources, respectively [24]. Some other nitrogen sources, such as polyacrylonitrile (PAN) [25], dopamine [26], and polyaniline [27], are also frequently added to carbon sources to fabricate nitrogen-doped carbon. Nevertheless, the complex polymerization (between nitrogen and carbon sources) and carbonization processes render the porosity uncontrollable, leading to a broad pore size distribution as well as low utilization of active material for charge storage. Thus, for the mass production of high performance supercapacitors, the fabrication of electrode material should be simple and scalable.

Biomass possesses many advantages, such as abundant natural reserves and environmental friendliness, and has drawn quickly intensive attention in the production of nitrogen-doped carbon materials [28-31]. As one of the biomass family, gelatin can be directly employed as the nitrogen and carbon source through thermal annealing [32,33]. For instance, Fan et al. obtained nitrogen-doped carbon nanosheets via the hydrothermal treatment of gelatin and graphene oxide mixed solution, followed by a chemical activation process to give microporous channels [8]. Other reports on gelatin-derived nitrogen-doped carbon are also available [14,34-37]. However, the resultant carbonaceous materials typically demonstrate irregular porous channels and a broad pore size distribution. So, engineering nitrogen-doped carbons with ordered porous channels through a simple but scalable route would be quite necessary, but has proven to be challenging [38].

Herein, we report on the scalable production of nitrogen-doped carbon sheets with ordered mesoporous channels. We achieved this

---

†To whom correspondence should be addressed.
E-mail: fanlei@yzu.edu.cn, hanjie@yzu.edu.cn

Copyright by The Korean Institute of Chemical Engineers.

through a simple casting of gelatin-silica nanospheres aqueous mixture, followed by carbonization and template removal. Neither polymerization nor chemical activation process is needed. By adjusting the sacrificial silica size as well as the carbonization temperature, the ordered porosity and nitrogen content can be correspondingly tuned. This allows us to screen the optimized conditions for achieving high performance charge storage device. The facile, scalable route to produce nitrogen-doped, ordered mesoporous carbon sheets may shed light on many applications, such as catalysis, water splitting, and rechargeable batteries.

## EXPERIMENTAL

### 1. Materials

Gelatin, ethanol ($CH_3CH_2OH$), ammonia ($NH_3 \cdot H_2O$) and NaOH were purchased from Sinopharm Chemical Reagent. Tetraethyl orthosilicate (TEOS) and $SiO_2$ nanospheres (10 nm, 20 nm) were purchased from Sigma-Aldrich. All chemicals above were of analytical grade. 50 nm and 100 nm $SiO_2$ nanospheres were synthesized by a typical modified Stöber method [39]: 0.8 mL ammonia was added to a mixture of 92 mL ethanol and 17.2 mL deionized water, which was magnetically stirred until completely mixed. Then 3.5 mL TEOS was added, followed by stirring for 3 h at 50 °C. After centrifugation, the sediment was obtained and washed for three times with deionized water and ethanol alternately. Finally, 100 nm $SiO_2$ nanospheres were obtained by drying in an oven at 60 °C overnight. 50 nm $SiO_2$ nanospheres were prepared in the same manner where the added ammonia was reduced to 0.7 mL.

### 2. Synthesis of Gelatin/$SiO_2$ Mixture

0.5 g gelatin was dispersed in 25 mL deionized water and stirred at 60 °C until completely dissolved. $SiO_2$ nanoparticles (diameter= 20 nm) were dissolved in the deionized water and ultrasonically homogenized to obtain a 40 wt% $SiO_2$ dispersion. Afterwards, 0.625 g of the $SiO_2$ dispersion was added to the gelatin solution, followed by stirring at 60 °C for 1 hour. After cooling, the mixture was cast on a glass plate and dried in an oven at 40 °C for 2 min. Finally, the film was scraped and labelled as Gelatin/$SiO_2$.

### 3. Synthesis of Nitrogen-doped Porous Carbon Sheet Materials

After purging with the $N_2$ flow for 20 min, the Gelatin/$SiO_2$ powders were heated to 800 °C with a ramping rate of 5 °C/min, held for 2 h, and labelled as SC-20-800, where "20" and "800" represent the diameter of $SiO_2$ and carbonization temperature, respectively. The pyrolysis process turns the gelatin into carbon decorated with $SiO_2$. To remove the $SiO_2$ template and introduce ordered pores, the abovementioned carbonized powders were soaked in 40 mL 1 M NaOH solution at 80 °C for 2 h. After cooling to room temperature, they were washed with deionized water to neutrality, dried overnight at 60 °C, and labelled as NCSs-20-800, where "20" and "800" represent the diameter of $SiO_2$ and carbonization temperature, respectively. To examine the best condition for engineering nitrogen-doped carbon porous sheets, templates with different $SiO_2$ particle size ranging from ~10 nm to ~100 nm were employed at a constant pyrolysis temperature (800 °C). The samples are labelled as NCSs-x-800, where x indicates the diameter of $SiO_2$. Similarly, the pyrolysis temperature was varied from 600 °C to 1,000 °C at a constant $SiO_2$ size (20 nm), and labeled as NCSs-20-y, where y is carbonization temperature.

### 4. Characterization

The morphology of the NCSs was characterized by field-emission scanning electron microscopy (SEM, Zeiss-supra55 operated at 5 kV, German) and transmission electron microscopy (TEM, Tecnai-12 Philip Apparatus Co. operated at 120 kV, USA). X-ray powder diffraction (XRD, D8 ADVANCE using Cu K$\alpha$ radiation ($\lambda$=0.154 nm), German), Raman spectroscopy (Renishaw in Via Spectrometer equipped with a 532 nm laser), Elemental analysis (Vario EL cube elemental analyzer with a conventional CHN combustion method), X-ray photoelectron spectroscopy (XPS, Thermo ESCALAB 250Xi spectrometer with Al K$\alpha$ radiation (1,486.6 eV)), as well as Fourier transform infrared spectroscopy (FTIR, Bruker Spectroscopy Instrument) was carried out to analyze the composition, structure and surface characteristic. Porosity parameters of the NCSs were evaluated at 77 K through the nitrogen adsorption/ desorption measurements (Micromeritics ASAP 2020). The samples were degassed at 393 K in a vacuum line for at least 2 h before measurements. The Brunauer-Emmett-Teller (BET) method was used to calculate the specific surface area, and the pore size distribution and pore volumes were derived from the Barrett-Joyner-Halenda (BJH) model.

### 5. Electrochemical Measurements

The energy storage performance of the NCSs was tested in three-electrode and two-electrode configurations. Cyclic voltammetry (CV), galvanostatic charge/ discharge (GCD) and electrochemical impedance spectroscopy (EIS) at open-circuit potential (OCV) were tested on the VMP3 electrochemical workstation (Biologic, France). The as-synthesized nitrogen-doped porous carbon sheet and polytetrafluoroethylene were added to ethanol in a mass ratio of 95 : 5, ultrasonically dispersed, and further processed to a paste, which the working electrodes were punched. The working electrodes were 8 mm in diameter, 2 mg in mass with the 316 stainless steel as the current collector. Counter electrodes, with 13 mm diameter and 20 mg mass, were processed from YP-50 and polytetrafluoroethylene (in a mass ratio of 95 : 5) in ethanol. Ag/AgCl electrode was used as the reference electrode in the Swagelok® three-electrode system while 1 M $H_2SO_4$ solution was used as the electrolyte and Celgard as the separator. And 1 M $H_2SO_4$ was also used as the electrolyte in the two-electrode system. The specific capacitance, energy density and power density of the electrodes were calculated according to relevant formulas, as shown in supporting information.

## RESULTS AND DISCUSSION

### 1. Characterization

As described previously, we employed gelatin as the nitrogen/ carbon source and obtained the nitrogen-doped mesoporous carbon sheets upon a simple and scalable approach (Scheme 1). $SiO_2$ with different particle sizes were synthesized through a modified Stöber method [39] as shown in Fig. S1. In this work, four sizes (10 nm, 20 nm, 50 nm, 100 nm) $SiO_2$ were used as the sacrificial template to give NCSs with ordered pore channels. Dispersing $SiO_2$ nanoparticles in the gelatin solution gives a suspension which is viscous enough and can be directly cast onto the glass substrate (Fig. 1(a)-(b)). Upon naturally drying, a smooth film was formed

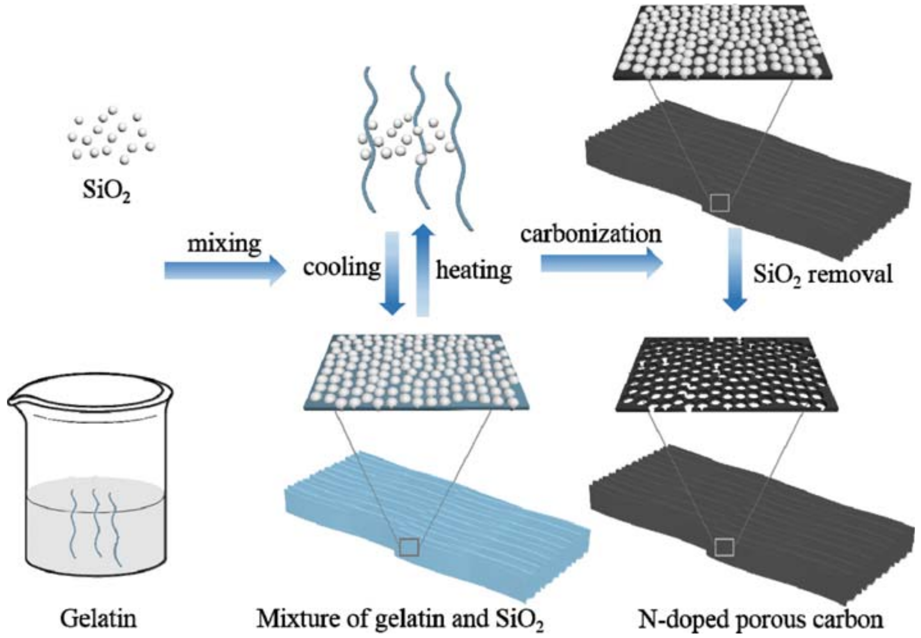

**Scheme 1. Schematic of the synthesis of nitrogen-doped carbon sheets (NCSs).**

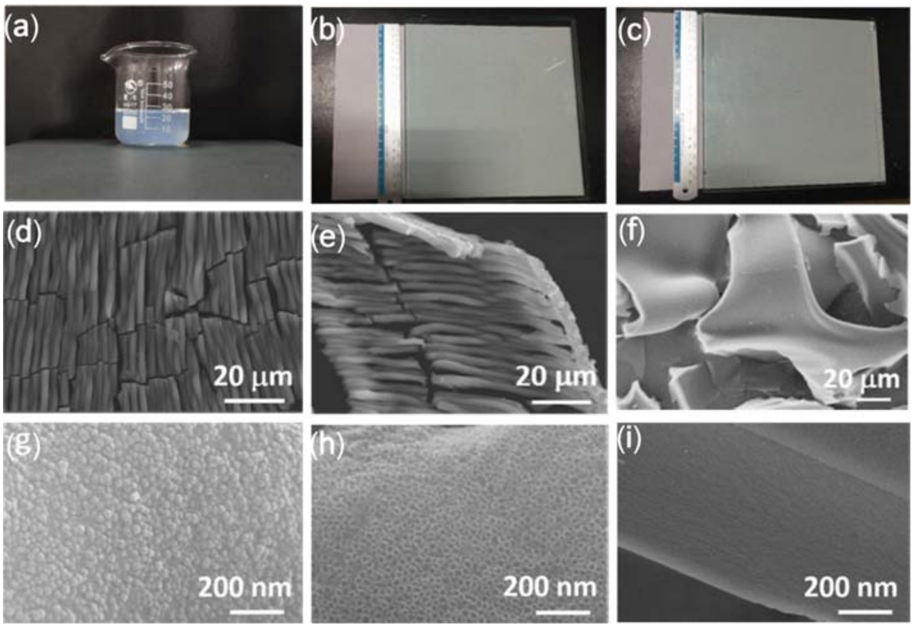

**Fig. 1. Optical images of (a) the mixture dispersion of gelatin and 20 nm $SiO_2$; Gelation-$SiO_2$-cast on a glass plate (b) before and (c) after drying; SEM images of carbonized samples (d)-(e) with $SiO_2$ added ((d), before and (e), after the removal of $SiO_2$) and (f) no $SiO_2$ added (NCSs-800). The patterns in (g)-(i) indicate the high magnification SEM images at corresponding conditions.**

(Fig. 1(c)). Further carbonization turns the gelatin into carbon while $SiO_2$ nanoparticles are preserved. Based on the low magnification SEM image (Fig. 1(d)), visible boundaries are found, forming continuous carbon sheets. Such a sheet structure may probably be due to the surface shrinkage caused by the addition of $SiO_2$. A closer examination from the high-magnification SEM image reveals that the carbonized material surface is homogeneously covered by numerous, evenly distributed particles (Fig. 1(g)) that are $SiO_2$ nanospheres. Upon soaking in NaOH, these $SiO_2$ nanospheres were removed and reverse, ordered porous channels appeared (Fig. 1(e), (h)). As a comparison, carbonizing pure gelatin film resulted in a nonporous carbon (NCSs-800) with a smooth surface (Fig. 1(f), (i)), suggesting the importance of $SiO_2$ in achieving ordered porous channels.

To illustrate the effect of $SiO_2$ particle size on the resultant carbon morphology, SEM and TEM studies were performed and

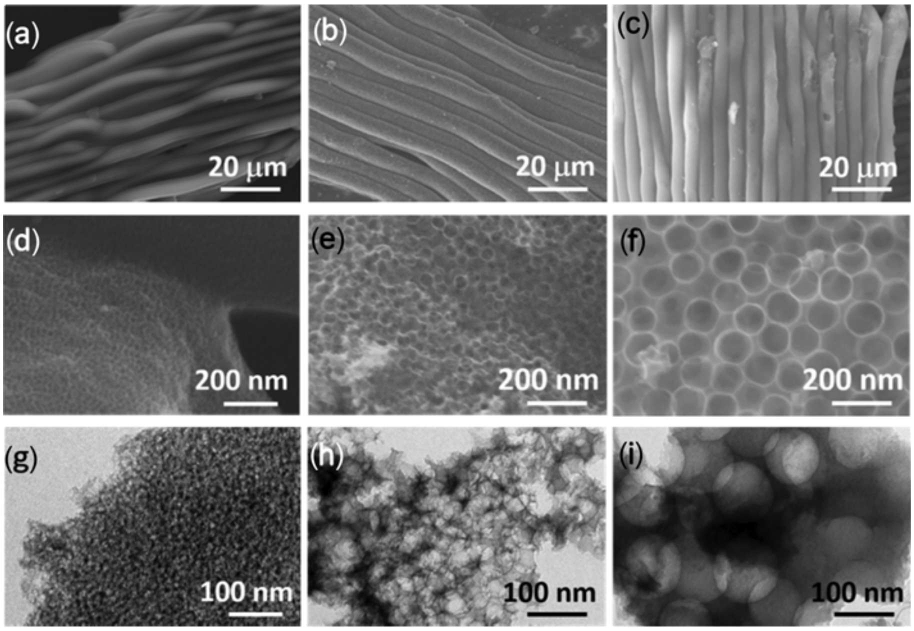

**Fig. 2.** **SEM images of (a), (d) NCSs-10-800; (b), (e) NCSs-50-800; (c), (f) NCSs-100-800; TEM patterns of (g) NCSs-10-800; (h) NCSs-50-800; (i) NCSs-100-800.**

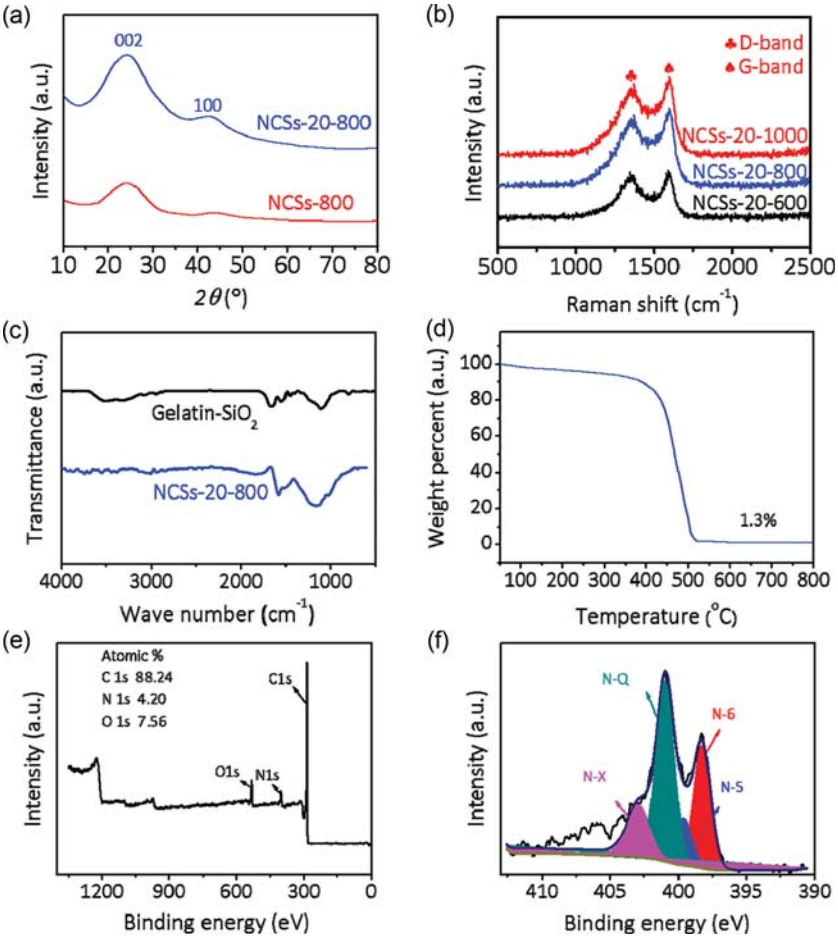

**Fig. 3.** **(a) XRD patterns of NCSs-800 and NCSs-20-800; (b) Raman spectrum of NCSs-20-y; (c) FTIR spectra of gelatin-SiO$_2$ and NCSs-20-800; (d) TGA curve of NCSs-20-800 sample; (e) XPS survey spectrum of NCSs-20-800; (f) High-resolution XPS spectrum of the deconvoluted N 1s peak.**

shown in Fig. 2. It can be clearly seen that $SiO_2$ particles were covered by the carbon after carbonizing at 800 °C (Fig. S2). In addition, the gelatin self-aligned into fibers and further assembled into sheets, which shrank considerably upon pyrolysis. After the removal of $SiO_2$, the sheet morphology was retained with numerous interconnected, pores inversely formed on the lamellar structure (Fig. 2(a)-(f)). These ordered, circular pores can be clearly seen from the SEM images (Fig. 2(d)-(f)) and TEM images (Fig. 2(g)-(i)). Note that the pore size is roughly similar as that of the template $SiO_2$ size (Fig. S3). For instance, removing the 10 nm and 100 nm $SiO_2$ nanospheres led to the formation of mesopores with an average pore size of 9.8 nm and 97 nm, respectively. All these reveal that the template removal process does not cause the collapse of the carbon nanostructure while maintaining the interconnected network. We note that such ordered, interconnected mesoporous channels are of unique importance for the fast ion transport kinetics, which will be discussed below.

The crystal structure of the sample was evaluated by X-ray diffraction (XRD). Two broad peaks centered at 26.4° and 43° can be ascribed to the (002) and (100) planes, respectively, of amorphous carbon (JCPDS 65-6212). The typical peak of $SiO_2$ (centering at 22°) is invisible in the XRD pattern, suggesting the residual $SiO_2$ content is negligible (Fig. 3(a)). The Raman spectrum of the NCSs-20-y (Fig. 3(b)) shows two peaks corresponding to the D-band and G-band peaks of the amorphous carbon, respectively. The peak area ratio ($I_D/I_G$) is lower than 1, suggesting a certain degree of graphitization in the carbonized sample. Fig. 3(c) shows the FTIR patterns of gelatin-$SiO_2$ and NCSs-20-800. It can be observed that the peaks centered at 3,400-3,500 $cm^{-1}$ in the Gelatin-$SiO_2$ correspond to the stretching vibration peaks of N-H. The peak of 1,044 $cm^{-1}$ was identified as the stretching vibration peak of Si-O, while the bending vibration peak of which was centered at 805 $cm^{-1}$ [40], indicative of the existence of $SiO_2$. The characteristic peak at 1,290-1,600 $cm^{-1}$ corresponds to the characteristic amide region of gela-

**Table 1. Porosity parameters and elemental analysis of different NCSs samples**

| Sample | Pores size (nm) | Surface area ($m^2$ $g^{-1}$) | Pore volume ($cm^3$ $g^{-1}$) | C (%) | N (%) | H (%) |
|---|---|---|---|---|---|---|
| NCSs-800 | 4.1 | 1.5 | 0.017 | 76.4 | 7.2 | 2.0 |
| NCSs-10-800 | 7.2 | 774.8 | 0.999 | 76.2 | 8.6 | 2.2 |
| NCSs-20-600 | 11.2 | 314.3 | 0.965 | 75.1 | 12.5 | 2.9 |
| NCSs-20-800 | 12.0 | 473.6 | 1.186 | 76.6 | 7.4 | 2.3 |
| NCSs-20-1000 | 11.6 | 304.0 | 0.988 | 78.5 | 2.1 | 1.3 |
| NCSs-50-800 | 4.1 | 141.2 | 0.473 | 76.4 | 6.8 | 2.2 |
| NCSs-100-800 | 4.1 | 30.9 | 0.407 | 76.0 | 6.4 | 2.5 |

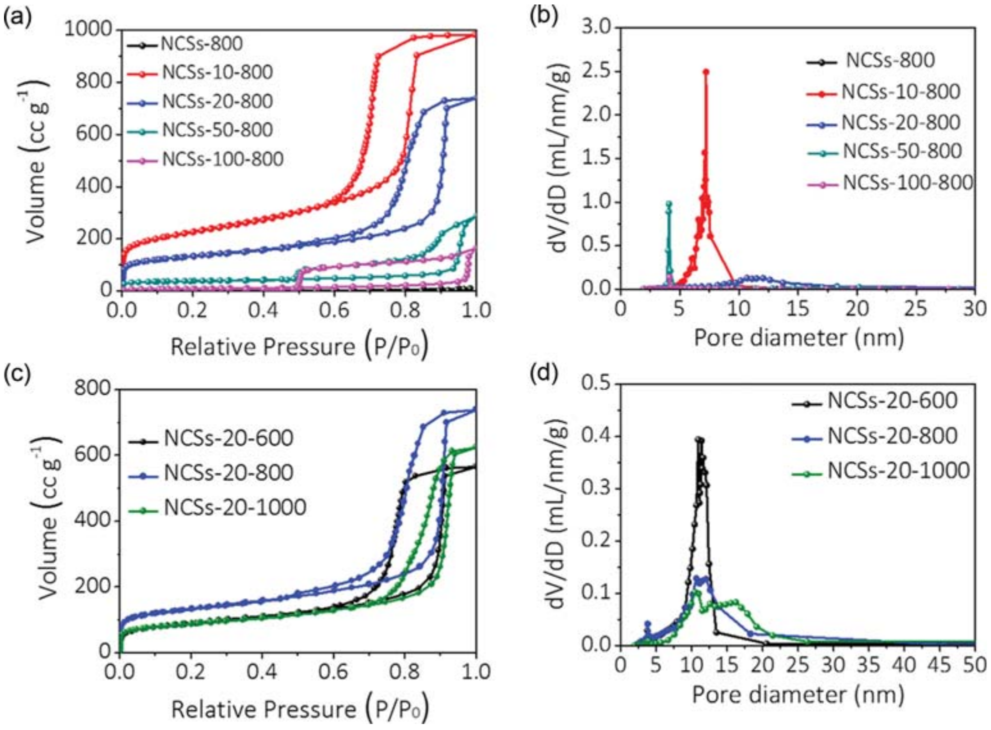

**Fig. 4.** (a) $N_2$ adsorption-desorption isotherms and (b) pore size distribution of nitrogen-doped carbon prepared with diverse $SiO_2$ particle sizes. The carbonization temperature was fixed at 800 °C; (c) $N_2$ adsorption-desorption isotherms and (d) pore size distribution of nitrogen-doped carbon prepared under different carbonization temperatures.

tin. After thermal pyrolysis and $SiO_2$ removal, the characteristic peaks of carbon (1,598 $cm^{-1}$ and 1,250 $cm^{-1}$) were found; the characteristic peaks of the gelatin as well as $SiO_2$ disappeared, suggesting that the $SiO_2$ nanospheres were effectively removed from the amorphous carbon. This can also be further verified by the TGA profile of the NCSs-20-800 sample (Fig. 3(d)), as an ash content of 1.3% was found. To determine the content of the doped-nitrogen, XPS analysis was performed on NCSs-20-800 (Fig. 3(e)-(f)). The survey in Fig. 3(e) suggests only C 1s, N 1s, and O 1s core-level were observed, with the nitrogen content of 4.2 at%. By tuning the $SiO_2$ particle size, the doped nitrogen content can be adjusted from 8.6 wt% to 6.3 wt%, as summarized in Table 1. The N 1s core level peak can be further deconvoluted into four peaks (Fig. 3(f)), corresponding to pyridinic-N (N-6,), pyrrolic-N (N-5), quaternary N (N-Q) and oxidized N (N-X) [41]. The prominent N-Q peak suggests 45% of the doped nitrogen located in the backbone of the carbon network, which is helpful in improving the surface wettability and electronic conductivity of the carbon material [42-44]. N-6 (30%) and N-5 (12%) are also reported to be beneficial to pseudocapacitance, thus further improving the capacitance of nitrogen-doped carbon materials [45,46].

The nitrogen sorption-desorption isotherms of NCSs prepared using different particle sizes of $SiO_2$ are shown in Fig. 4(a). From the shape of the isotherms (type IV), it is clear that some micropores exist when the template $SiO_2$ particle size is smaller than 20 nm, as seen by the abrupt increase in the absorption curve in the low relative pressure region ($P/P_0<0.05$). Further increasing the template size beyond 20 nm leads to a negligible number of microporous channels. The narrow pore size distribution (Fig. 4(b)) suggests the pores are primarily small mesopores. Interestingly, there is a bimodal behavior in the NCS-10-800 and NCS-20-800 (Fig. 4(b)) with the mean pore size of 7.2 nm and 12 nm (Table 1), reflecting the template effect of 10 nm and 20 nm $SiO_2$. One possible explanation could be that the shrinkage behavior results in the decreased pore size, compared to the size of $SiO_2$. Moreover, the mesoporous behavior of the NCS-50-800 and NCS-100-800 is attributed to the relatively large template size. In general, a larger sacrificial $SiO_2$ size results in a gradually decreased specific surface area (SSA), as demonstrated in Table 1. For instance, the SSA is 774.8 $m^2/g$ in the NCSs-10-800, and decreases to 30.9 $m^2/g$ in the NCSs-100-800. As a contrast, the NCSs-800 obtained from pyrolyzing the pure gelatin gives an SSA of 1.5 $m^2/g$ with a nitrogen content of 7.2 wt% (Table 1). On the other hand, the effect of carbonization temperature is of less significance on the porosity parameters of the NCSs, best seen in the similar isotherms and overlapping pore size distributions (Fig. 4(c)-(d)). The SSA of NCSs obtained at different carbonization temperature is also in the similar range (Table 1). However, the atomic percent of doped nitrogen changes significantly by adjusting the carbonization temperature. For instance, when pyrolyzed at 600 °C, the nitrogen content can be as high as 12.5 wt%, in sharp contrast to 2.1 wt% at a pyrolyzing temperature of 1,000 °C (Table 1).

## 2. Electrochemical properties

To quickly check the effect of introduced porosity on the elec-

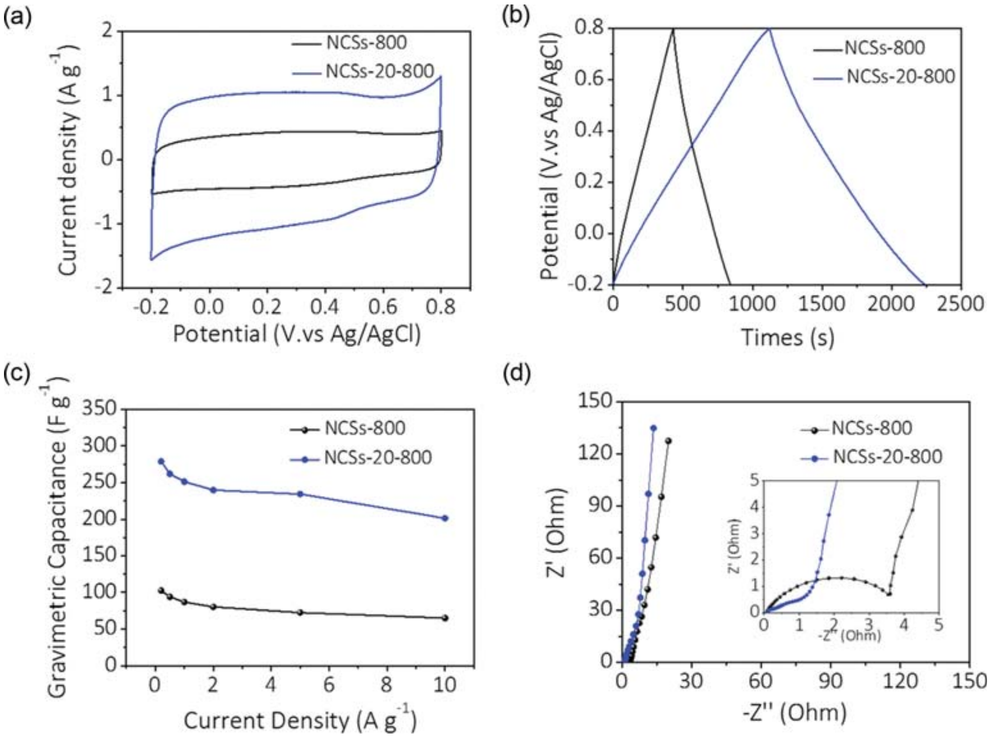

**Fig. 5. Electrochemical performance of NCSs-800 and NCSs-20-800 using a three-electrode configuration with 1 M $H_2SO_4$ as the electrolyte. (a) CV curves between −0.2 and 0.8 V at a scan rate of 5 mV $s^{-1}$, (b) Charge-discharge curves at a current density of 0.2 A $g^{-1}$, (c) Specific capacitances of NCSs-800 and NCSs-20-800 calculated from charge-discharge curves, (d) Nyquist plots of NCSs-800 and NCSs-20-800; inset shows the Nyquist plot in the high frequency region.**

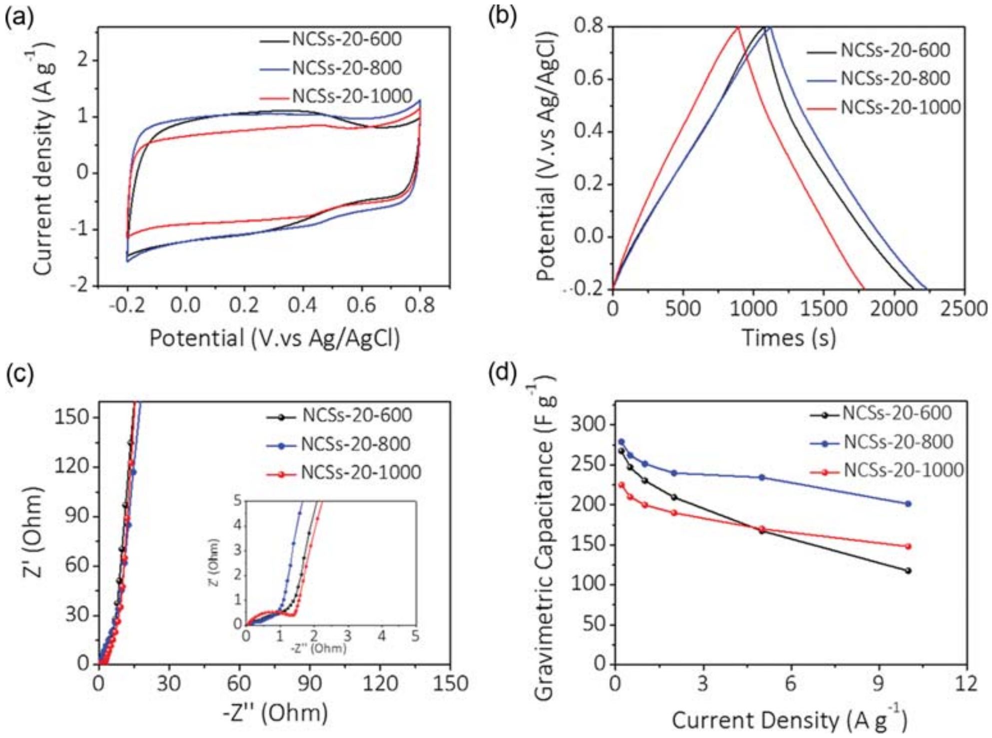

**Fig. 6. (a)-(d) Electrochemical responses of NCSs-20-y with (a) CVs at 5 mV s$^{-1}$, (b) GCDs at 0.2 A g$^{-1}$, (c) Nyquist plots (Inset shows the plot in the high frequency region) and (d) specific capacitance calculated from charge-discharge curves.**

trochemical response of the NCSs, two types of NCSs, NCSs-800 and NCSs-20-800, were compared, as these two samples have similar nitrogen content but dramatically different porosities (and as a result, SSA). Fig. 5(a) displays the cyclic voltammograms (CVs) of these two samples at 5 mV s$^{-1}$, exhibiting quasi-rectangular CV shape as expected. The broad anodic and cathodic peak couple (locating at −0.2 to 0.5 V, vs Ag/AgCl) in both samples can be attributed to the fast-redox reactions between acidic nitrogen-containing sites and protons from the electrolyte [47]. The pseudocapacitive behavior can also be verified by the quasi-linear galvanostatic charge-discharge (GCD) profiles in Fig. 5(b). In addition, the symmetric triangular GCD curves suggest a high Coulombic efficiency in both NCSs [48]. Compared to NCSs-800 which is nonporous, NCSs-20-800 possesses developed mesoporous, ordered channels that are beneficial for achieving a fast ion transport kinetics. Consequently, attributed to the multi-porous system, a larger integrated area in the CV curve and a prolonged discharge time are obtained, indicative of much higher capacitance. As shown in Fig. 5(c), with the current density of 0.2 A g$^{-1}$, the specific capacitance of NCSs-20-800 is 278 F g$^{-1}$, superior to 103 F g$^{-1}$ of NCSs-800. With increasing the current density to 10 A g$^{-1}$, NCSs-20-800 retains a high capacitance of 210 F g$^{-1}$ while the specific capacitance of NCSs-800 decreases to 71 F g$^{-1}$. The improved capacitance retention in NCSs-20-800 (76% as increasing the current density by 50-fold) can be fairly attributed to the ordered mesoporous channels with a narrow pore size distribution, allowing a fast ion diffusion kinetics and improving the utilization of active materials for pseudocapacitive energy storage [49]. This point can be further verified by the electrochemical impedance spectroscopy (EIS). As shown in the inset of Fig. 5(d), the semicircle at a high frequency region, representing the charge-transfer resistance ($R_{ct}$), is 0.9 Ω in NCSs-20-800 but increases to 3.5 Ω in nonporous NCSs-800. In addition, the curve at a low frequency region is steeper in the NCSs-20-800 than NCSs-800, indicative of an improved ion diffusion kinetics and better active material utilization, agreeing well with the rate handling capability analysis (Fig. 5).

We then studied the influences brought by carbonization temperature on the electrochemical response. As seen in Fig. 6(a)-(c), all samples exhibit quasi-rectangular CV shapes, quasi-linear GCD profiles, and almost vertical Nyquist plots at the low frequency region, indicative of the mixed behavior of both double-layer capacitance and pseudocapacitance [50]. The maximum capacitance achieved in the NCSs-20-800 reaches 278 F g$^{-1}$ at 0.2 A g$^{-1}$, exceeding the rest of NCSs and suggesting that carbonization temperature of 800 °C is the optimized condition to give the highest capacitance (Fig. 6(d)). Note that, at 1 A g$^{-1}$, the capacitance of NCSs-20-800 is 252 F g$^{-1}$, surpassing most other nitrogen-doped mesoporous carbons at similar mass loading and current density, as demonstrated in Table 2. In addition, NCSs-20-600 possesses a similar capacitance at that of NCSs-20-800 at 0.2 A g$^{-1}$, but decays quickly as the current density increases beyond 0.2 A g$^{-1}$ (Fig. 6(d)). We note that, besides a much higher nitrogen content (12.5 wt%) in NCSs-20-600, the porosity parameters of NCSs-20-y samples are quite similar. Thus, the difference in the rate handling of NCSs-20-600 and NCSs-20-800 can be fairly attributed to the poor electronic conductivity. This point also agrees with the conclusions from Long et al., who revealed that that excessive doped nitrogen would interrupt the electronic network of the carbonized sample,

**Table 2. Comparison of the specific capacitances of NCSs-20-800 and other reported Nitrogen-doped carbon materials**

| Sample | SC[a] (F $g^{-1}$) | m[b] (mg) | J[c] (A $g^{-1}$) | Electrolyte | Ref. |
|---|---|---|---|---|---|
| NCSs-20-800 | 252 | 2 | 1 | 1 M $H_2SO_4$ | This work |
| Carbon nanobelts | 233 | 3 | 1 | 6 M KOH | [45] |
| Nitrogen-doped carbon fiber | 195 | 1 | 1 | 1 M $H_2SO_4$ | [33] |
| N,P co-doped hollow carbon microspheres | 175 | 3 | 1 | 6 M KOH | [52] |
| N-doped porous carbon nanofibers | 198 | 1.5 | 1 | 6 M KOH | [53] |
| N-doped carbon spheres | 231 | 3 | 1 | 6 M KOH | [54] |
| Graphene | 180 | 2 | 1 | 6 M KOH | [55] |
| Hierarchically porous carbon | 213 | 2.4 | 1 | 6 M KOH | [56] |
| Porous carbon aerogel | 185 | 1.6 | 1 | 1 M $H_2SO_4$ | [57] |

[a] SC: specific capacitance

[b] m: the mass of the active substance

[c] J: current density

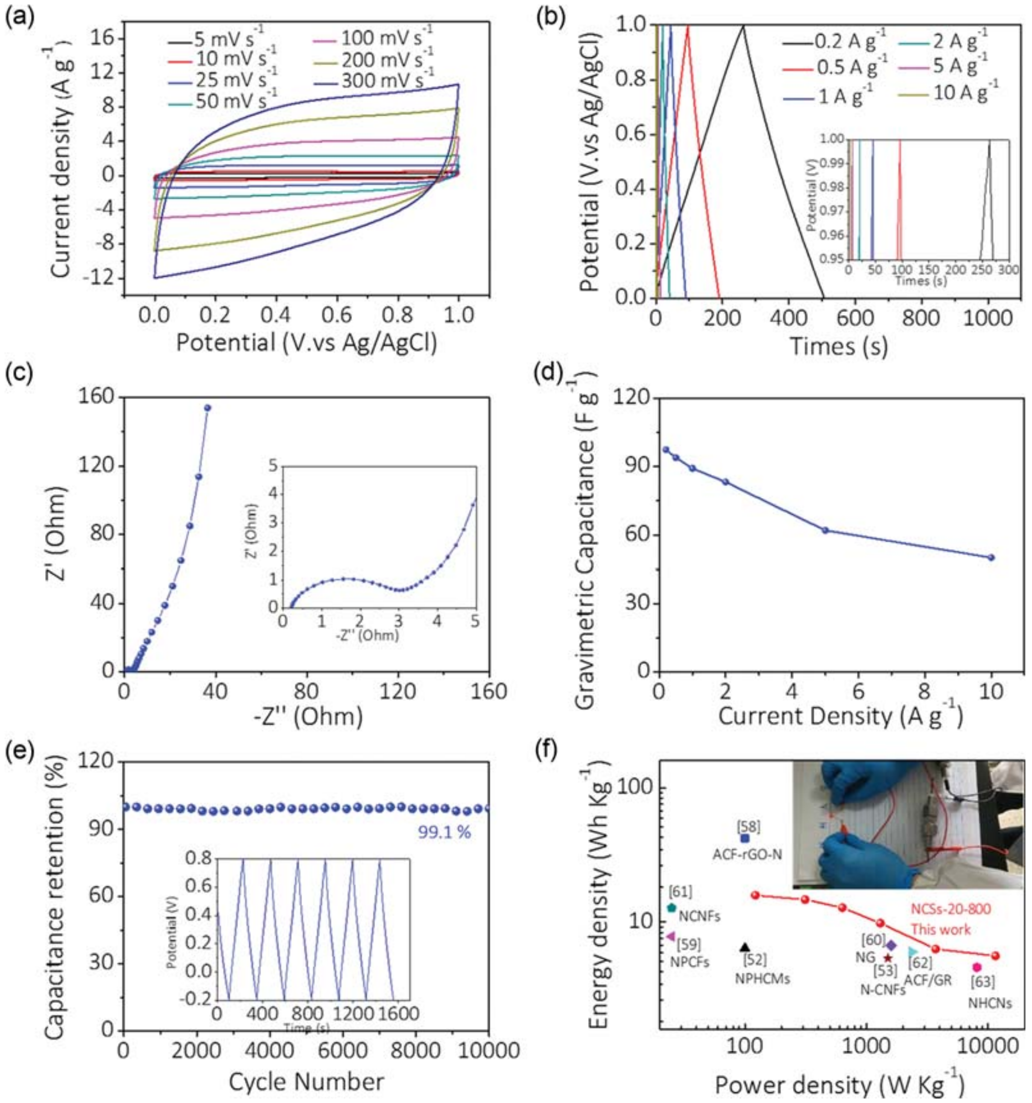

**Fig. 7.** **Electrochemical performance of the symmetric supercapacitor assembled by pairing up two identical NCSs-20-800 electrodes. (a) CV curves at different scan rates. (b) Charge-discharge curves at different current densities, inset shows the negligible IR drop. (c) Nyquist plot at the open circuit (inset shows the plot at medium-high frequency range). (d) The specific capacity at different current densities. (e) Cycling stability (the inset is typical charge-discharge curves during cycling) at a current density of 1 A $g^{-1}$. (f) Ragone plot of the symmetric device. Inset shows the prototype device in powering the light-emitting diode (LED).**

and lower the electronic conductivity as a result [24]. Interestingly, NCSs-20-1000 demonstrates lower capacitances than NCSs-20-800 in the entire current density range but decent capacitance retention. This can be explained by the much reduced nitrogen content (2.1 wt%), as well as the smaller specific surface area (304 $m^2$/g) (Table 1), leading to much fewer redox active sites for charge storage. Consequently, the charge-transfer resistance ($R_{ct}$) is even larger than that of NCSs-20-600, as shown in the inset of Fig. 6(c). On the other hand, raising the carbonization temperature is known as an effective method to improve the electronic conductivity by introducing certain degree of graphitization of the carbonaceous materials [51], resulting in superior rate handling of NCSs-20-1000 (Fig. 6(d)). Influence of sacrificial template size on the electrochemical responses of NCSs can be found in Fig. S4, showing similar pseudocapacitive behavior and confirming that 20 nm $SiO_2$ is the optimized size for achieving both high capacitance and excellent rate capability.

Finally, we demonstrate the potential of our nitrogen-doped ordered mesoporous carbon for energy storage by evaluating the electrochemical performance of symmetric device based on NCSs-20-800 electrodes. As shown in Fig. 7(a)-(b), the quasi-rectangular CV curves and linear GCD profiles suggest a good capacitive response within a voltage window of 1 V. Moreover, at a scan rate of 300 mV $s^{-1}$, the CV curve quickly stabilized upon the voltage reversal, suggesting the ideal capacitive behavior was well maintained at a high rate. This point can be further verified by the negligible IR drop at 10 A $g^{-1}$ (inset of Fig. 7(b)) as well as the vertical Nyquist plot at the low frequency region (Fig. 7(c)). Consequently, the NCSs-20-800 demonstrates excellent cycling lifetime, which retains 99.1% of the initial capacitance after 10000 cycles (Fig. 7(e)). No parasitic reactions were involved in the charge storage, best seen by the symmetric quasi-linear GCD curves (inset of Fig. 7(e)) and high Coulombic efficiency (~100%). The maximum energy density and power density of the symmetric device reached 15.8 Wh $kg^{-1}$ and 11.5 kW $kg^{-1}$, respectively (Fig. 7(f)). Except nitrogen-doped carbon fiber/reduced graphene oxide (ACF-rGO-N), which showcased a higher energy density of 42 Wh $kg^{-1}$ [58], our symmetric device has surpassed most other supercapacitors based on nitrogen-doped carbons [52,53,59-63], such as nitrogen-doped graphene (NG) (6.7 Wh $kg^{-1}$) [60], nitrogen-phosphorus co-doped hollow carbon microspheres (NPHCMs) (6.4 Wh $kg^{-1}$) [52], and nitrogen-doped carbon nanofibers (NCNFs) (12.1 Wh $kg^{-1}$) [61], etc., as detailed in Fig. 7(f). We believe that the facile low-cost synthesis of nitrogen-doped ordered mesoporous carbon holds great promise in the production of future energy storage devices for various applications, such as powering LEDs (inset of Fig. 7(f)).

## CONCLUSIONS

We prepared nitrogen-doped, ordered mesoporous carbon sheets by a simple and scalable method in which the gelatin serves as carbon/nitrogen source and $SiO_2$ nanospheres as the template. By a low-cost solution casting of gelatin-silica mixture, the gelatin molecules self-aligned into regular sheets, which turned into ordered, mesoporous carbon sheets with a narrow pore size distribution after further carbonization and template removal. The nitrogen content and porosity parameters can be effectively adjusted by tuning the silica size and/or pyrolysis temperature. The narrow pore size distribution, coupled with active nitrogen sites, renders the nitrogen-doped carbon sheets with good charge storage performance, including a high specific capacitance, good rate handling, and high energy/power density. While we are not aiming for achieving nitrogen-doped carbons with the highest capacitance/energy density, we specifically focused on simple and low-cost synthesis of nitrogen-doped carbon sheets with an ordered pore structure. Such a synthesis route and material design may find various applications, including water splitting, catalysis and lithium-sulfur batteries, with promising performance.

## ACKNOWLEDGEMENTS

This work was supported by the National Natural Science Foundation of China (NO. 21001091, 21673202), the Project Funded by the Priority Academic and the University Natural Science Foundation of Jiangsu Province (16KJD150004). We would also like to acknowledge the technical support received at the testing center of Yangzhou University.

## SUPPORTING INFORMATION

Additional information as noted in the text. This information is available via the Internet at http://www.springer.com/chemistry/journal/11814.

## REFERENCES

1. D. W. Wang, F. Li, M. Liu, G. Q. Lu and H. M. Cheng, *Angew. Chem., Int. Ed.*, **47**, 373 (2008).
2. M. F. El-Kady, V. Strong, S. Dubin and R. B. Kaner, *Science*, **335**, 1326 (2012).
3. T. Chen and L. M. Dai, *Mater. Today*, **16**, 272 (2013).
4. T. Chen and L. M. Dai, *J. Mater. Chem. A*, **2**, 10756 (2014).
5. K. Li and J. T. Zhang, *Sci. China Mater.*, **61**, 210 (2018).
6. P. B. Liu, M. Y. Yang, S. H. Zhou, Y. Huang and Y. D. Zhu, *Electrochim. Acta*, **294**, 383 (2019).
7. R. R. Salunkhe, C. Young, J. Tang, T. Takei, Y. Ide, N. Kobayashi and Y. Yamauchi, *Chem. Commun.*, **52**, 4764 (2016).
8. H. L. Fan and W. Z. Shen, *ACS Sustainable Chem. Eng.*, **4**, 1328 (2015).
9. J. Y. Tian, C. Y. Liu, C. Lin and M. Y. Ma, *J. Alloys Compd.*, **789**, 435 (2019).
10. J. Yu, M. Y. Guo, F. Muhammad, A. F. Wang, F. Zhang, Q. Li and G. S. Zhu, *Carbon*, **69**, 502 (2014).
11. M. Seredych, J. Jagiello and T. J. Bandosz, *Carbon*, **74**, 207 (2014).
12. J. Y. Tian, H. Y. Zhang, Z. M. Liu, G. Qin and Z. H. Li, *Int. J. Hydrogen Energy*, **43**, 1596 (2018).
13. Y. H. Lee, Y. F. Lee, K. H. Chang and C. C. Hu, *Electrochem. Commun.*, **13**, 50 (2011).
14. H. Y. Jia, H. Zhang, S. Wan, J. W. Sun, X. Xie and L. T. Sun, *J. Power Sources*, **433**, 226712 (2019).
15. Z. Jin, J. Yao, C. Kittrell and J. M. Tour, *ACS Nano*, **5**, 4112 (2011).
16. D. Hulicova-Jurcakova, M. Kodama, S. Shiraishi, H. Hatori, Z. H.

Zhu and G. Q. Lu, *Adv. Funct. Mater.*, **19**, 1800 (2009).

17. C. Y. Zhang, X. H. Zhu, M. Cao, M. L. Li, N. Li, Q. Q. Lai, J. L. Zhu and D. C. Wei, *ChemSusChem*, **9**, 932 (2016).
18. E. Samuel, B. Joshi, M. W. Kim, Y. I. Kim, M. T. Swihart and S. S. Yooh, *Chem. Eng. J.*, **371**, 657 (2019).
19. Y. J. Ji, Y. L. Deng, H. M. Wu and A. X. Tong, *J. Appl. Electrochem.*, **49**, 599 (2019).
20. W. Yang, W. Yang, L. N. Kong, A. L. Song, X. J. Qin and G. J. Shao, *Carbon*, **127**, 557 (2018).
21. X. C. Chen, R. Paul and L. M. Dai, *Natl. Sci. Rev.*, **4**, 453 (2017).
22. K. L. Van Aken, M. Beidaghi and Y. Gogotsi, *Angew. Chem., Int. Ed.*, **54**, 4806 (2015).
23. C. F. Zhang, R. Maloney, M. R. Lukatskaya, M. Beidaghi, B. Dyatkin, E. Perre, D. H. Long, W. M. Qiao, B. Dunn and Y. Gogotsi, *J. Power Sources*, **274**, 121 (2015).
24. H. C. Chen, F. G. Sun, J. T. Wang, W. C. Li, W. M. Qiao, L. C. Ling and D. H. Long, *J. Phys. Chem. C*, **117**, 8318 (2013).
25. K. B. Huang, M. Li, Z. H. Chen, Y. Y. Yao and X. W. Yang, *Electrochim. Acta*, **158**, 306 (2015).
26. Q. W. Wu, G. We, Z. B. Xu, J. Han, J. Q. Xi, L. Fan and L. Z. Gao, *ACS Appl. Mater. Interfaces*, **10**, 25026 (2018).
27. A. M. Shrivastav, G. Sharma, A. S. Rathore and R. Jha, *ACS Photonics*, **5**, 4402 (2018).
28. E. Ruiz-Hitzky, M. Darder, F. M. Fernandes, E. Zatile, F. J. Palomares and P. Aranda, *Adv. Mater.*, **23**, 5250 (2011).
29. Y. L. Deng, Y. J. Ji, H. M. Wu and F. Chen, *Chem. Commun.*, **55**, 1486 (2019).
30. W. Du, X. N. Wang, J. Zhan, X. Q. Sun, L. T. Kang, F. Y. Jiang, X. Y. Zhang, Q. Shao, M. Y. Dong, H. Liu, V. Murugadoss and Z. H. Guo, *Electrochim. Acta*, **296**, 907 (2019).
31. V. Strauss, K. Marsh, M. D. Kowal, M. El-Kady and R. B. Kaner, *Adv. Mater.*, **30**, 1704449 (2018).
32. Z. R. X. Guan, H. Liu, B. Xu, X. Hao, Z. X. Wang and L. Q. Chen, *J. Mater. Chem. A*, **3**, 7849 (2015).
33. L. Fan, L. Yang, X. Y. Ni, J. Han, R. Guo and C. F. Zhang, *Carbon*, **107**, 629 (2016).
34. X. Y. Chen, C. Chen, Z. J. Zhang and D. H. Xie, *J. Mater. Chem. A*, **1**, 10903 (2013).
35. B. Xu, S. S. Hou, F. L. Zhang, G. P. Cao, M. Chu and Y. S. Yang, *J. Electroanal. Chem.*, **712**, 146 (2014).
36. A. Olejniczak, M. Lezanska, A. Pacula, P. Nowak, J. Wloch and J. P. Lukaszewicz, *Carbon*, **91**, 200 (2015).
37. Y. H. Qu, Z. A. Zhang, X. H. Zhang, G. D. Ren, Y. Q. Lai, Y. X. Liu and J. Li, *Carbon*, **84**, 399 (2015).
38. H. L. Fan and W. Z. Shen, *Chemsuschem*, **8**, 2004 (2015).
39. J. B. Joo, Q. Zhang, I. Lee, M. Dahl, F. Zaera and Y. D. Yin, *Adv. Funct. Mater.*, **22**, 166 (2012).
40. W. X. Shu, J. P. Zheng, T. Lei and D. Y. Kang, *J. Appl. Polym. Sci.*, **101**, 1556 (2006).
41. M. Zhou, F. Pu, Z. Wang and S. Y. Guan, *Carbon*, **68**, 185 (2014).
42. T. Q. Lin, I. W. Chen, F. X. Liu, C. Y. Yang, H. Bi, F. F. Xu and F. Q. Huang, *Science*, **350**, 1508 (2015).
43. J. H. Hou, C. B. Cao, F. Idrees and X. L. Ma, *ACS Nano*, **9**, 2556 (2015).
44. L. Yao, Q. Wu, P. X. Zhang, J. M. Zhang, D. R. Wang, Y. L. Li, X. Z. Ren, H. W. Mi, L. B. Deng and Z. J. Zheng, *Adv. Mater.*, **30**, 1706054 (2018).
45. T. Ouyang, K. Cheng, F. Yang, L. M. Zhou, K. Zhu, H. Ye, G. L. Wang and D. X. Cao, *J. Mater. Chem. A*, **5**, 14551 (2017).
46. L. J. Xie, G. H. Sun, F. Y. Su, X. Q. Guo, Q. Q. Kong, X. M. Li, X. H. Huang, L. Wan, W. Song, K. X. Li, C. X. Lv and C. M. Chen, *J. Mater. Chem. A*, **4**, 1637 (2016).
47. L. Fei, B. P. Williams, S. H. Yoo, J. M. Carlin and Y. L. Joo, *Chem. Commun.*, **52**, 1501 (2015).
48. H. L. Guo and Q. M. Gao, *J. Power Sources*, **186**, 551 (2009).
49. S. Abouali, M. A. Garakani and J. K. Kim, *Electrochim. Acta*, **284**, 436 (2018).
50. S. J. He and W. Chen, *J. Power Sources*, **262**, 391 (2014).
51. P. B. Geng, S. S. Zheng, H. Tang, R. M. Zhu, L. Zhang, S. Cao, H. G. Xue and H. Pang, *Adv. Energy Mater.*, **8**, 1703259 (2018).
52. N. Zhang, F. Liu, S. D. Xu, F. Y. Wang, Q. Yu and L. Liu, *J. Mater. Chem. A*, **5**, 22631 (2017).
53. X. L. Li, Y. J. Zhao, Y. Bai, X. Y. Zhao, R. H. Wang, Y. C. Huang, Q. H. Liang and Z. H. Huang, *Electrochim. Acta*, **230**, 445 (2017).
54. J. G. Wang, H. Z. Liu, H. H. Sun, W. Hua, H. W. Wang, X. R. Liu and B. Q. Wei, *Carbon*, **127**, 85 (2018).
55. B. You, J. H. Jiang and S. J. Fan, *ACS Appl. Mater. Interfaces*, **6**, 15302 (2014).
56. P. Cheng, S. Y. Gao, P. Y. Zang, X. F. Yang, Y. L. Bai, H. Xu, Z. H. Liu and Z. B. Lei, *Carbon*, **93**, 315 (2015).
57. X. Tian, S. Zhu, J. Peng, Y. T. Zuo, G. Wang, X. H. Guo, N. Q. Zhao, Y. Q. Ma and L. Ma, *Electrochim. Acta*, **241**, 170 (2017).
58. X. M. Qiu, Z. C. Xiao, L. N. Wang and L. Z. Fan, *Carbon*, **130**, 196 (2018).
59. L. F. Chen, X. D. Zhang, H. W. Liang, M. G. Kong, Q. F. Guan, P. Chen, Z. Y. Wu and S. H. Yu, *ACS Nano*, **6**, 7092 (2012).
60. F. M. Hassan, V. Chabot, J. D. Li, B. K. Kim, L. Ricardezsandoval and A. P. Yu, *J. Mater. Chem. A*, **1**, 2904 (2013).
61. A. Choudhury, J. H. Kim, S. S. Mahapatra, K. S. Yang and D. J. Yang, *ACS Sustainable Chem. Eng.*, **5**, 2109 (2017).
62. Q. X. Xie, S. H. Wu, Y. F. Zhang and P. Zhao, *J. Electroanal. Chem.*, **801**, 57 (2017).
63. J. N. Zhang, X. L. Zhang, Y. C. Zhou, S. J. Guo, K. X. Wang, Z. Q. Liang and Q. Xu, *ACS Sustainable Chem. Eng.*, **2**, 1525 (2014).

# Supporting Information

## Facile and scalable synthesis of nitrogen-doped ordered mesoporous carbon for high performance supercapacitors

**Lei Fan[†], Peizheng Sun, Li Yang, Zhilong Xu, and Jie Han[†]**

School of Chemistry and Chemical Engineering, Yangzhou University, Yangzhou 225002, China

(*Received 24 August 2019 • accepted 21 October 21*)

**Electrochemical calculation formula**

In the three-electrode system, the specific capacitance of the electrodes was calculated from the GCD curves according to equation:

$$C_{spe}=\frac{I\times\Delta t}{m\times\Delta V}=\frac{j\times\Delta t}{\Delta V} \qquad (1)$$

Where $C_{spe}$ (F $g^{-1}$) is the specific capacitance, j (A $g^{-1}$) is the current density, Δt (s) is the discharge time, ΔV (V) is the potential window excluding the IR-drop and m (g) is the mass of the working electrode.

In the two-electrode device with the identical YP-50 as the positive and negative electrodes, the specific capacitance was calculated according to the following equation:

$$C_{spe}=\frac{4I\times\Delta t}{M\times\Delta V} \qquad (2)$$

where M (g) is the total mass of the active materials on the both electrodes in the device, I (A) is the discharging current. The specific capacitance was also calculated from the CV integration according to equation:

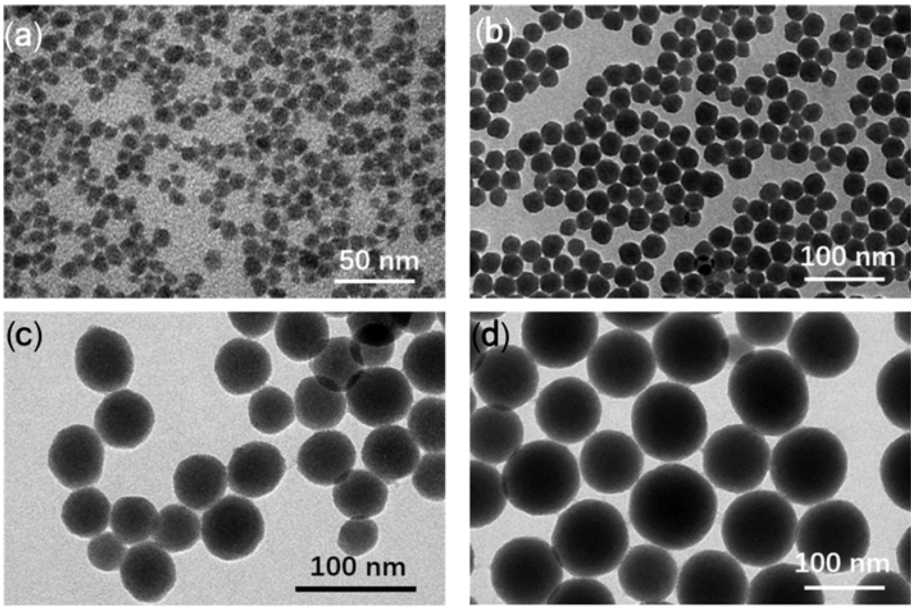

**Fig. S1. SEM patterns of different size of $SiO_2$ (a) 10 nm; (b) 20 nm; (c) 50 nm; (d) 100 nm.**

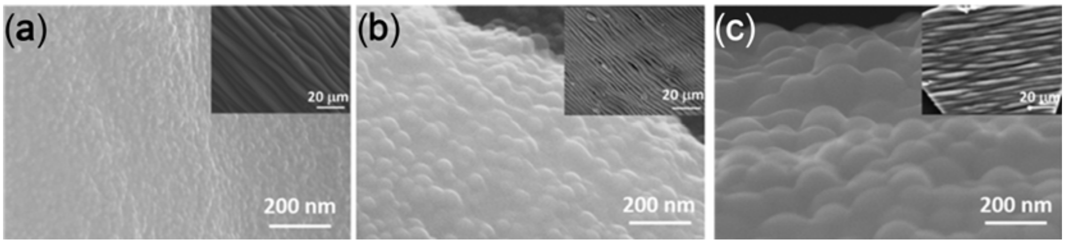

**Fig. S2. SEM patterns of (a) SC-10-800; (b) SC-50-800; (c) SC-100-800.**

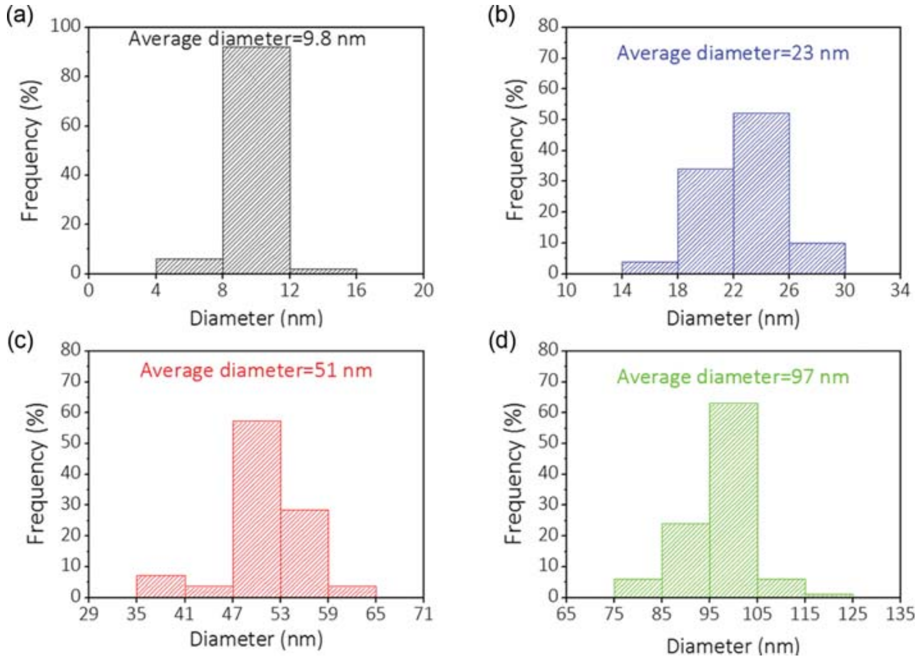

**Fig. S3. Size distribution of different size of $SiO_2$ (a) 10 nm; (b) 20 nm; (c) 50 nm; (d) 100 nm.**

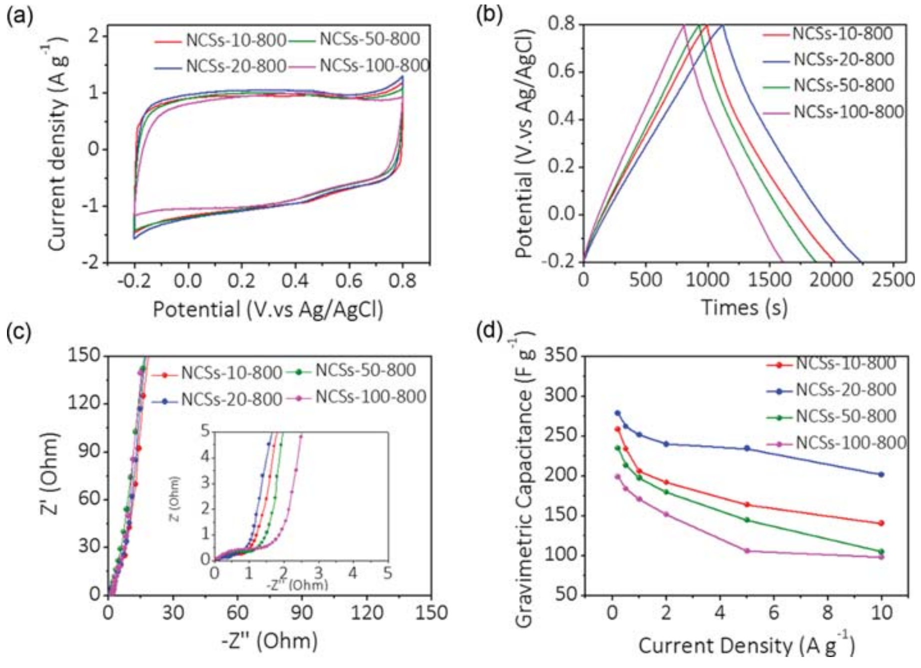

**Fig. S4. (a)-(d) Electrochemical responses of NCSs-x-800 with (a) CVs at 5 mV $s^{-1}$, (b) GCDs at 0.2 A $g^{-1}$, (c) Nyquist plots (inset shows the plot in the high frequency region) and (d) specific capacitance calculated from charge-discharge curves.**

$$C_{spe}=\frac{2\int idV}{vm\Delta V} \tag{3}$$

where m is mass of one electrode, v is the scan rate.

The energy density and power density of a supercapacitor were determined by the following equations:

$$E_t=\frac{1}{2}C_{spe}\times\Delta V^2\times\frac{1}{3.6} \tag{4}$$

$$P_t=\frac{E_t\times 3600}{\Delta t} \tag{5}$$

Where $E_t$ (W h $kg^{-1}$) is the specific energy density, $P_t$ (W $kg^{-1}$) is the specific power density, $C_{spe}$ (F $g^{-1}$) is the specific capacitance based on the total device system, ΔV (V) represents the discharge voltage range exclusive of the IR drop and Δt (s) is the discharge time.